Progress In Electromagnetics Research, Vol. 167, 19–30, 2020

Multi-Objective Genetic Algorithm Optimization of Frequency Selective Metasurfaces to Engineer Ku-Passband Filter Responses

Kenneth W. Allen*, Daniel J. P. Dykes, David R. Reid, and Richard T. Lee

Abstract—Metasurfaces enable a new avenue to create electrically thin multi-layer structures, on the order of one-tenth the central wavelength (λ_c), with engineered responses. Altering the sub-wavelength spatial features, e.g., $\lambda_c/80$, on the surface leads to highly tunable electromagnetic scattering characteristics. In this work, we develop an ultra-wideband frequency selective metasurface (FSmS) that completely encompasses the Ku-band from 12–18 GHz with steep band edges. The geometrical structure of the metasurfaces is optimized by a multi-objective genetic algorithm mimicking evolutionary processes. Analysis is performed from one- to four-layer metasurface structures with various thicknesses. Computational electromagnetic simulations for these frequency selective metasurfaces are presented, discussed, and experimentally validated. The concepts presented in this work can be applied to design metasurfaces and metamaterials from the microwave to the optical regimes.

1. INTRODUCTION

Electromagnetic scattering can be controlled by engineering sub-wavelength spatial features, either in a plane or volume, corresponding to metasurfaces and metamaterials, respectively. Initially, these man-made structures were investigated as effective homogenous media, because as the lattice constant is sufficiently smaller than the impinging wavelength (λ) [1, 2]. Since the seminal articles on metamaterials and metasurfaces, researchers have been galvanized to explore the fundamental physics and device applications [3–7]. Significant focus has been on the use of metamaterials to synthesize materials with magnetic responses [2] and negative indices of refraction [3] for applications ranging from invisibility cloaks [5] to super-resolution [8]. Recently, non-linear metasurfaces have been engineered by integrating electronic components into the cellular structure, which enables the ability to promote phenomena such as power- and waveform-dependent responses [9–14]. The integration of electrical components can also allow for tunable metasurfaces for dispersion compensation [15]. However, metasurface advancements have not been limited to active components and include deviations from effective medium models to manipulate diffractive modes. Passive metasurfaces have been engineered to control the wavefront for effects spanning planar optics [16–19] to efficient scattering into higher order Floquet harmonics from the RF- [20, 21] to THz-regimes [22, 23].

Metasurfaces, i.e., planar metamaterials of electrical thicknesses $< \lambda$, can offer the ability to finely tune the scattering response; thus, enabling frequency-selectivity within the fundamental Floquet harmonic ($m = 0$, $n = 0$). Recently, there has been piqued interest in FSSs for K-band due to an assortment of applications [24–26]. In this work, we demonstrate an ultra-wideband frequency selective metasurface (FSmS) bandpass filter encompassing the Ku-band (12–18 GHz) with low insertion loss, steep roll off features for high out-of-band rejection, and robust angular responses. In Section 2, physical bounds are placed on the search space and fitness functions are determined by implementing

Received 26 November 2019, Accepted 31 January 2020, Scheduled 23 February 2020
* Corresponding author: Kenneth W. Allen (kenneth.allen@gtri.gatech.edu).
The authors are with the Advanced Concepts Laboratory, Georgia Tech Research Institute, Georgia Institute of Technology, 30332, USA.

theoretical limitations (e.g., Bode-Fano theory). Computational electromagnetic (CEM) results from finite-difference time-domain (FDTD) simulations, operating on a high performance computing (HPC) cluster, coupled with an optimizer based on evolutionary processes are analyzed. In addition, the optimum FSmS designs from the FDTD simulations are imported into a finite-element method (FEM) solver to simulate the angular response of the FSmSs. Experimental validation is provided in Section 3. This paper ends with brief conclusions on FSmS design guidelines in Section 4.

2. COMPUTATIONAL ELECTROMAGNETICS

2.1. Metasurfaces Guided by Evolution

Charles Darwin's theory of evolution, by natural selection or survival of the fittest, has proven to be a concept that transcends biological systems. Genetic algorithms (GAs) utilize evolutionary processes, Figure 1, that can be successfully implemented as a powerful design tool for the generation and characterization of electromagnetic structures and materials [27–30].

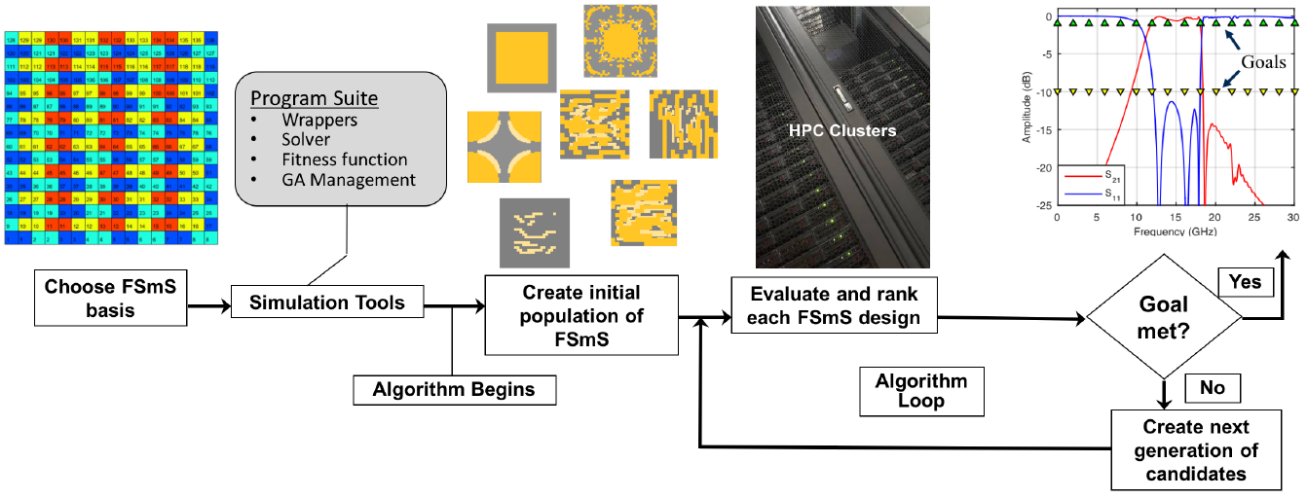

Figure 1. Schematic illustration for the concept of evolutionary process used for FSmS designs.

Our implementation of GA optimized FSmS structures is an iterative process bounded by basic physics estimations and design constraints, which is illustrated in Figure 1. First, an appropriate basis set is selected for the model, and this basis is encoded as a binary sequence. The size of the FSmS period (Λ) is determined by constraints of the diffracted orders (e.g., $\Lambda < \lambda_c/2$ to conserve energy in specular order, where λ_c is the center wavelength of the Ku-band). The discretization within the period is a compromise between ability to finely tune the surface and the desire to reduce the number of bits introduced into the search space. Also, symmetry conditions can be forced within the period to reduce the search space or to promote particular polarization responses. In the propagation direction, the FSmS is bound to the available thickness for a given application or fabrication capabilities, whichever is the limiting factor. After the basis set has been selected, an appropriate CEM solver is selected. In this study, ultra-wideband frequency content is being studied; therefore, an FDTD solver is a good choice since the Fourier transformed time domain signal provides the response for all frequencies of interests in a single run. In addition to the CEM solver, the parameters of the multi-objective GA are set (e.g., mutation rate, population sizes, etc.). Fitness functions are mathematically described to guide the desired performance, and any post-processing wrappers to analyze results are incorporated. An initial population of FSmS can then be implemented based on previous simulations or canonical shapes with a known response similar to the desired performance. However, in this work, the initial population set was not seeded with previous designs or canonical forms in order to ensure the GA selection process was not artificially biased or forced into a local minimum of the search space. This process is coupled with

a HPC architecture that can efficiently evaluate numerous simulations and generations for convergence of solutions.

In our work, the metasurface unit cell structure is encoded in the GA using a binary string where "1's" and "0's" correspond to perfect electric conductor (PEC) and free-space, respectively. The analogy follows that the string of binary code is a chromosome, and the binary constituents are the genes. In the initial population group, there are 50 chromosomes that are comprised of randomly generated genes. These chromosomes are then evaluated in regards to fitness; the desired response is described as a mathematical function. The fitness value is an indicator of the quality of the chromosome and decides whether that set of genes will be allowed to propagate. If selected the genes may undergo slight mutation, with a mutation rate of 1%, and evolve into new generations. Guided by that evolutionary process, new generations will converge towards an optimal solution.

In order to achieve convergence towards an optimal solution, the fitness function needs to be carefully considered and based on physical limits. For example, the in-band reflection goal was determined by following the procedure described in [31], Equation (1), where the theoretical match is determined for a passive system by the Bode-Fano limit, results shown in Figure 2.

$$\frac{\Delta f}{f_c}\ln\left(\frac{1}{|\Gamma_b|}\right) \leq \frac{c_0}{t(\epsilon_r - 1)f_c}. \tag{1}$$

This ensures that the optimizer is scoring for an in-band reflection ($|\Gamma_b|$) goal that is physically realizable. Otherwise, the fitness can force a search for solutions which cannot exist within the solution space. The fitness function ($\mathcal{F}$) is piecewise comprised of multiple components to generate ultra-wideband selectivity from the FSmS, as shown below:

$$\mathcal{F} = c_{\mathrm{IB}}x\left(\delta_{S_{21}}^{\mathrm{IB}} + \delta_{S_{11}}^{\mathrm{IB}}\right) + c_{\mathrm{OBL}}x\left(\delta_{S_{21}}^{\mathrm{OBL}} + \delta_{S_{11}}^{\mathrm{OBL}}\right) + c_{\mathrm{OBH}}x\left(\delta_{S_{21}}^{\mathrm{OBH}} + \delta_{S_{11}}^{\mathrm{OBH}}\right). \tag{2}$$

$\delta_{S_{21}}^{\mathrm{IB}}$ is the difference between the calculated and desired in-band (IB) transmitted (S_{21}) amplitudes, and $\delta_{S_{11}}^{\mathrm{IB}}$ is the difference between the calculated and desired in-band reflected (S_{11}) amplitudes. Similar quantities are defined for the lower out-of-band frequency range (OBL) and upper out-of-band frequency range (OBH). For this study these quantities are frequency independent numbers and the goals are ${S_{21}}^{\mathrm{IB}} = 0\,\mathrm{dB}$ (i.e., *perfect transmission*), ${S_{11}}^{\mathrm{IB}} = -12\,\mathrm{dB}$, ${S_{21}}^{\mathrm{OBL}} = {S_{21}}^{\mathrm{OBH}} = -12\,\mathrm{dB}$, and ${S_{11}}^{\mathrm{OBL}} = {S_{11}}^{\mathrm{OBH}} = 0\,\mathrm{dB}$ (i.e., *perfect reflection*). The frequency bands are 0–11.5 GHz, 12–18 GHz, and 18.5–30 GHz for OBL, IB, and OBH, respectively. This conservative in-band reflection goal was determined by inspection of Figure 2 based on the Bode-Fano limit analysis. In order to compensate for the bandwidth of the out-of-band scoring, the in-band fitness component is multiplied by a weighting

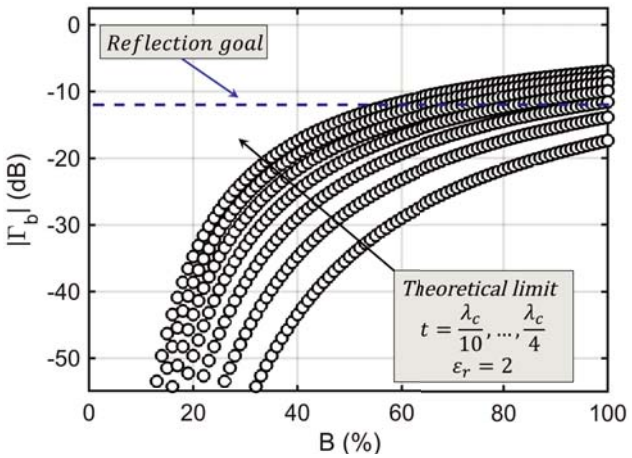

Figure 2. Bode-Fano theoretical limit for matching in-band reflection coefficient (Γ_b) of FSmS designs in free-space of thicknesses varying from $\lambda_c/4$ to $\lambda_c/10$ with $\epsilon_r = 2$ as a function of bandwidith, where $B = \Delta f/f_c \times 100\%$.

coefficient (i.e., $c_{\mathrm{IB}} = 2$), whereas the out-of-band coefficients (c_{OBL} and c_{OBH}) were set to unity. It should be noted that scaling coefficients can be instrumental to shaping and designing the FSmS's filter response. These scaling coefficients can be used to weight the significance of a particular frequency band more heavily. However, the general structure of the spectral response is dependent on the form of the fitness function.

FDTD simulations were performed with periodic boundary conditions (PBCs) in the plane of the FSmS, $x_{\min}$, $x_{\max}$, $y_{\min}$, and $y_{\max}$ planes, Figure 3(a). In order to electromagnetically truncate the computational volume, perfectly matched layers (PMLs) were assigned to the $z_{\min}$ and $z_{\max}$ planes, Figure 3(a). The computational volume of the grid was variable along $\hat{z}$, to accommodate a range of thicknesses for the FSmS from 0.5–5.0 mm. Therefore, largest computational volume corresponds to a FSmS thickness of 5 mm, i.e., $16 \times 16 \times 80$ Yee cells.

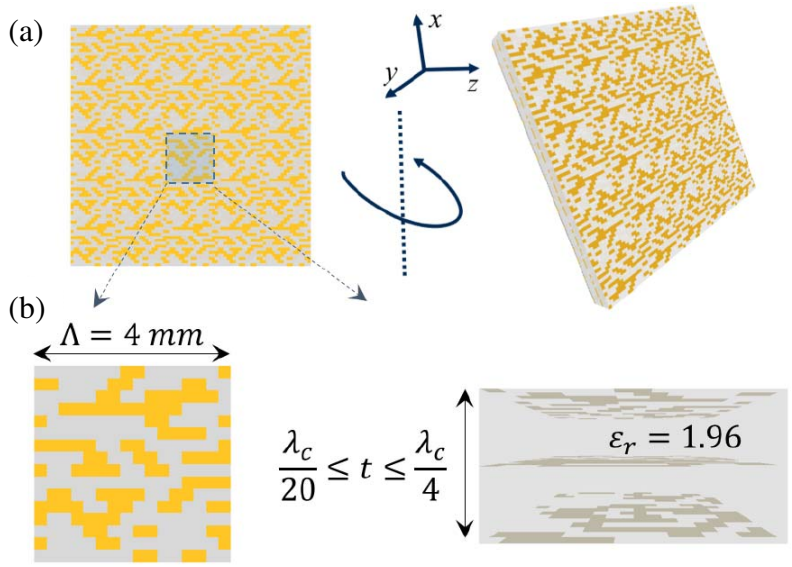

Figure 3. (a) Unit cell of the FSmS arrayed 5×5 to illustrate an array prototype at views of $\hat{z}$ normal and an oblique angle. (b) FSmS unit cell properties.

The unit cell of the FSmS has a period $\Lambda = 4\,\mathrm{mm}$ ($\lambda_c/5$), illustrated in Figure 3, ensuring transmitted power is conserved in the 0th order mode, i.e., no higher order diffracted modes will be excited in the frequency band of interest. However, higher order diffraction modes will be excited above 40 GHz. The complex permittivity ($\widetilde{\epsilon_r} = 1.96 - j0.001$) of the dielectric spacers was selected to match the electrical properties of Rogers 5880LZ, Figure 3(b), as a realistic material model for the CEM simulations. Low-permittivity substrates are superior to high-permittivity substrates in regards to bandwidth [33]. The size of the pixel's side length that the GA will be able to individually address on the metasurface is 250 µm (i.e., $\lambda_c/80$).

That level of discretization enables the 16×16 unit cell to be divided into 136 pixels per layer (n), where each pixel is 2×1 Yee cells. These pixels can be toggled between dielectric and PEC to manipulate and tune the response during the optimization. The metallization pattern on each layer can be unique from that of any other layer. The thickness of the FSmS, along the propagation direction, is allowed to vary from $\lambda_c/20$ to $\lambda_c/4$ in a discrete number (N) of $\lambda_c/80$ increments, Figure 3(b). This results in $(2N)^{136n}$ configurable states for a FSmS containing N thicknesses and n layers; a search space too vast to explore all possible configurations. The power of evolution guided design procedures is the ability to identify local minima in vast search spaces and push their depths to eventually achieve the global minimum, due to the stochastic nature of the process. It should be noted, this stochastic process is not directionless or a random walk [27]. In [32] this feat was shown to be achievable with rapid convergence without evaluating the entire search space for a 24-bit system for a fragmented antenna aperture.

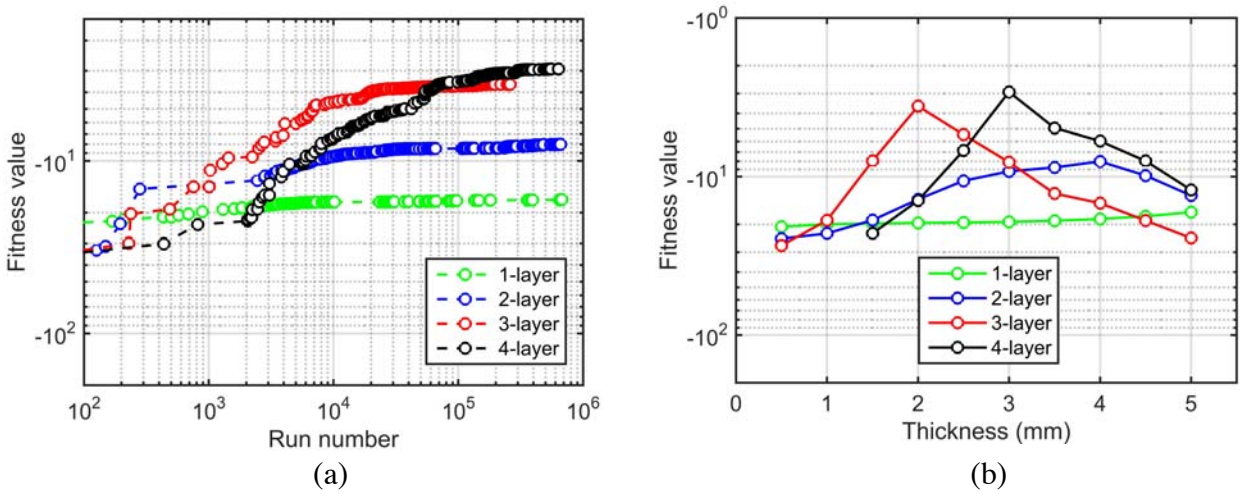

Figure 4. (a) Evolution of the FSmS performance, as described by the fitness function, over a duration of nearly one-million runs. (b) Multi-objective trade space of fitness and overall thickness of the FSmS structure.

Nearly 10^6 runs were performed for FSmS consisting of 1- to 4-layers, as shown in Figure 4. Dramatic improvements in the fitness value occur over the first 10^4 runs with instances of punctuated equilibrium; however, the slope begins to taper and converge by approximately 10^5 runs, as illustrated in Figure 4(a). A multi-objective GA was employed such that the Pareto-frontier can be monitored within the search space. In applications, frequency selective surfaces often have restrictions on thickness either due to the available physical footprint or fabrication capabilities. In this work, the multi-objective GA illustrates the interplay of the trade-space for this critical parameter and the performance of the FSmS, as shown in Figure 4(b).

The optimization-based design procedure is driven by the extrinsic performance of the metasurfaces, i.e., the reflection and transmission performance. It is often useful, however, when analyzing the performance of the metasurfaces designed by this process, to think about the structures in terms of their effective intrinsic properties, such as permittivity, permeability, or impedance. Considering the intrinsic properties of the metasurfaces, the trade space can be conceptually understood by using transmission line concepts. The product of the permittivity (ϵ_r) of the dielectric spacer and geometric thickness (t) between the metasurfaces can be tuned to impedance match the multi-layer structure (Z_{FSmS}) to the free-space impedance (Z_0) across the Ku-band. The capacitance of the metasurface dictates the low-pass component of the filter; similarly, the inductance controls the high-pass function. The combination of the FSmS's resistance (R), inductance (L), and capacitance (C) shape the overall spectral response of the FSmS. The evolution guided FDTD simulations alter the conductive topology of the metasurfaces that effectively tune the R, L, C values to optimize performance, as described by the fitness function. Each layer of the metasurface corresponds to a transmission pole, and consequently reflection null, which can be spectrally tuned by the GA to provide optimum overlap for minimum insertion losses and out of band rejection. The dependence of the FSmS performance on overall thickness and number of constituent layers is illustrated in Figure 4(b). The "best" performing FSmSs are considered in the next subsection.

2.2. Analysis of Selected Designs at Normal Incidence

The GA had converged towards optimal designs after well-over 10^5 FDTD simulations for 1–4 metasurface layer FSmSs had been performed, as shown in Figure 5. In this section, the best performing designs will be analyzed.

For the single-layer FSmS, Figure 5(a), S_{11} and S_{21} at the central frequency, λ_c, surpass the targeted goals, as shown in Figure 5(a). However, as the scattering parameters (S-parameters) are examined for frequencies extending beyond the λ_c, it can be seen that the performance is significantly degraded

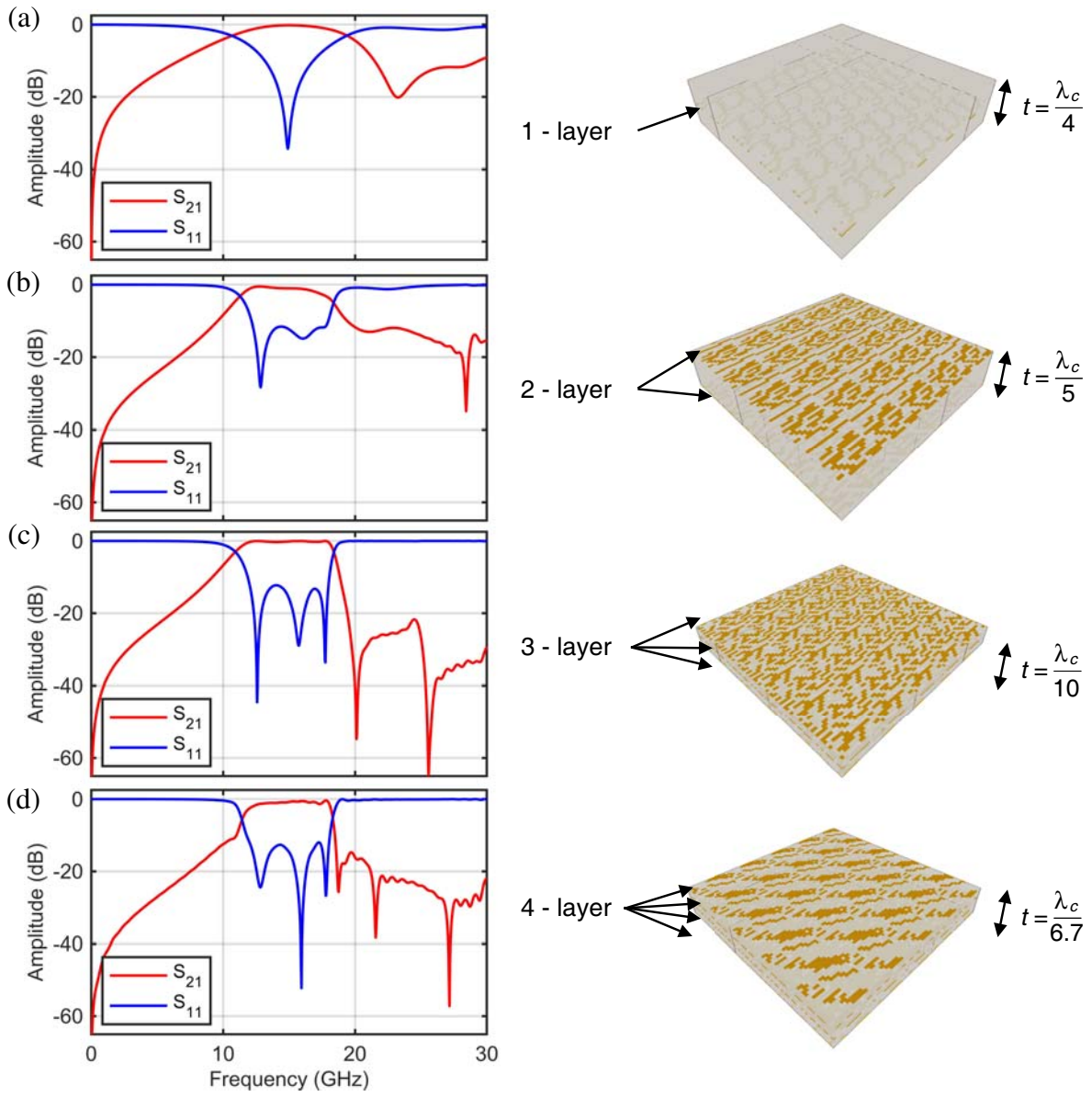

Figure 5. Oblique view of the optimized FSmS unit cell (arrayed 5 × 5 as an illustration) and corresponding spectral response of the transmitted (S_{21}) and reflected (S_{11}) scattering parameters for normal incidence of the electromagnetic wave with the structure for (a) 1-layer, (b) 2-layer, (c) 3-layer, and (d) 4-layer metasurfaces.

and the roll-off is undesirably gradual. This is due to the lack of transmission poles generated by the single layer FSmS. The thickness of this design is $\lambda_c/4$, i.e., 5 mm, which is the upper limit allowed by the GA. It should be noted, as shown in Figure 4(b), that the single-layer structure was impacted the least by the thickness of the substrate. It is known for electrically thin substrates that the operating frequency is scaled by a maximum value of the $\sqrt{\epsilon_r}$ fully embedded in a host medium or $\sqrt{\frac{\epsilon_r+1}{2}}$ for a single side [33]. The slight variation in performance as a function of thickness is suspected to be a manifestation of this scaling.

The two-layer FSmS was formed by adding another metasurface such that there is a layer on the top and bottom of the dielectric spacer, Figure 5(b). These two metasurfaces use independent fragmented metalized layers; consequently this increases the search space by an additional 136 bits. Since there are

two transmission poles, one for each layer, the impedance match of the FSmS and free-space is extended to a wider bandwidth, Figure 5(b), compared to the single-layer FSmS. Also, the roll-off between the in-band and out-of-band region is steeper in comparison with the single-layer FSmS. The thickness of

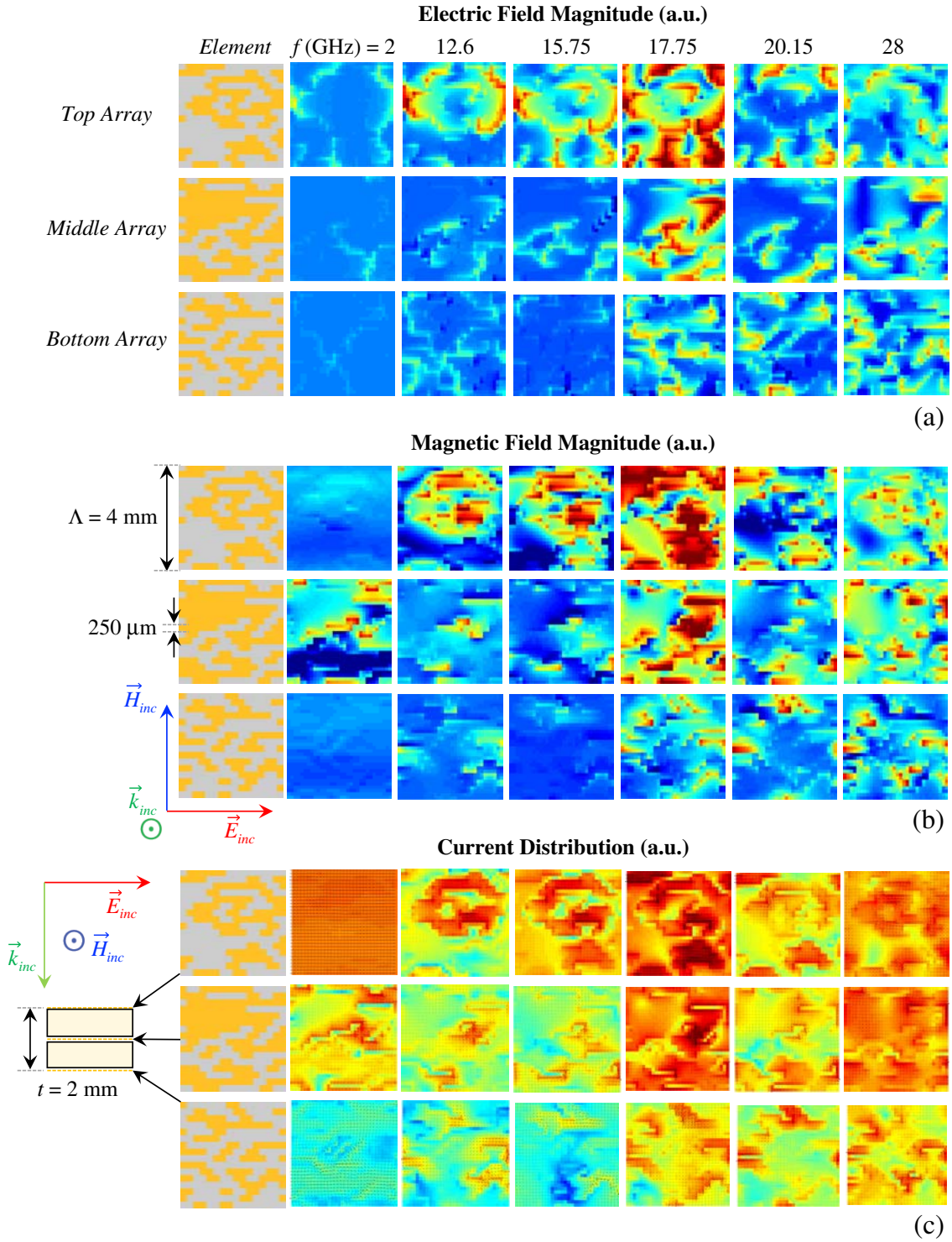

Figure 6. (a) Electric field, (b) magnetic field, and (c) approximate surface current distribution of the three-layers that combine to form the FSmS are shown. Element pattern details are illustrated along with stack up details and illumination conditions.

the FSmS has been reduced to $\lambda_c/5$ or 4 mm. It is also observed that impedance matching the layers for the two-layer FSmS structure is more sensitive to the overall thickness, Figure 4(b), in comparison to the single-layer FSmS.

Extending to a three-layer FSmS, in addition to the two fragmented layers placed on the top and bottom of the dielectric spacer, a third fragmented layer is inserted into the middle of the FSmS, Figure 5(c). This middle metasurface layer is allowed to vary independently of the top and bottom layers, further expanding the search space. Across the entire Ku-band, the insertion loss is less than 0.3 dB, Figure 5(c), outperforming all other FSmS presented in this article. In regards to the in-band reflection, it is better than −12 dB across the entirety of the Ku-band. The roll-off for the out-of-band lower frequency regime is similar to the two-layer FSmS case; however, the out-of-band higher frequencies regime is a sharp roll-off function, Figure 5(c). The three-layers were optimized such that the transmission poles were spaced optimally to reduce the in-band ripple of the passband response, this can be observed in 5(c) by the deep reflection nulls in-band. This three-layer FSmS not only has enhanced performance but the thickness has been reduced significantly to $\lambda_c/10$ or 2 mm.

Continuing, a four-layer FSmS, Figure 5(d), with four independent fragmented layers were equidistantly spaced along the propagation direction ($\hat{z}$) was optimized by evolutionary processes. Due to the discretization of the computational volume along the thickness, the four-layer FSmS required a thickness $\geq$ 1.5 mm, Figure 4(b). The performance of the four-layer FSmS was superior to the one- and two-layer FSmS. However, the overall performance was comparable with the three-layer FSmS with higher insertion losses (−2 dB maximum in-band insertion loss) but better roll-off, Figure 5(d). The four-layer FSmS had a larger overall electrical thickness of $\lambda_c/6.7$ or 3 mm in comparison with the three-layer FSmS structure at $\lambda_c/10$ or 2 mm. For completeness, a five-layer FSmS with five independent fragmented layers, similar to the four-layer FSmS, alternating along the propagation direction ($\hat{z}$) was optimized. The discretization of the metasurface along the thickness, did not allow for a five-layer structure until 1.25 mm of thickness. The performance of the five-layer FSmS structure was also comparable to the three- and four-layer FSmS. The insertion losses in-band peaked at 0.4 dB, slightly worse than the 0.3 dB of the three-layer FSmS, the roll-off of the five-layer FSmS was slightly better than the three-layer FSmS, but not as sharp as the four-layer FSmS with an overall electrical thickness of the five-layer FSmS was optimized to $\lambda_c/8$ or 2.5 mm.

Based on the normal incidence scattering characteristics results presented in Figure 5, the three-layer FSmS was selected for prototyping to validate the simulated results. In order to provide more detailed information and physical insight on the interaction of the impinging electromagnetic wave with the FSmS, field maps were generated for the electric and magnetic field magnitudes and the approximate surface current distribution as shown in Figure 6. The frequencies chosen for Figure 6 correspond to strong electromagnetic interactions with the FSmS. A frequency was selected corresponding to the lower frequency reflection band, i.e., 2 GHz. The three transmission pole frequencies field maps were calculated, i.e., 12.6, 15.75, and 17.75 GHz along with the transmission null at 20.15 GHz. Finally, a frequency (28 GHz) within the high frequency reflection band was mapped. The array element patterns for each of the three-layers are also illustrated in Figure 6 along with the composite stack up. It should be noted, these distributions were not the direct focus of the engineering effort but merely a consequence of designs scored by scattering performance of the FSmS.

2.3. Angular Responses of Optimized Metasurfaces

In addition to FDTD simulations at normal incidence, the 'best' FSmS designs for the 1- to 4-layer structures were also modeled with FEM simulations in order to investigate the angular response. Similar to the FDTD simulations the unit cell, Figure 3, was simulated with PBC surrounding the plane of the FSmS at the $x_{\min}$, $x_{\max}$, $y_{\min}$, and $y_{\max}$ planes. The same dimensions were used to grid the FEM and FDTD computational volume, 250 µm cubic mesh. The meshed geometry, including the pixelated layers, was imported into the FEM environment to be modeled. The FEM simulations were performed over a range of frequencies from 1 GHz to 30 GHz with a spectral resolution of $\sim$ 500 MHz and over a span of angles ranging from 0° to 60° with an angular resolution of $\sim 2°$, resulting in the S-parameter maps in Figure 7. The electric-field vector ($\vec{E_y}$) is oriented such that the observed polarization state is transverse-electric (TE) with respect to the plane of incidence over the range of incident angles, Figure 3(a). That

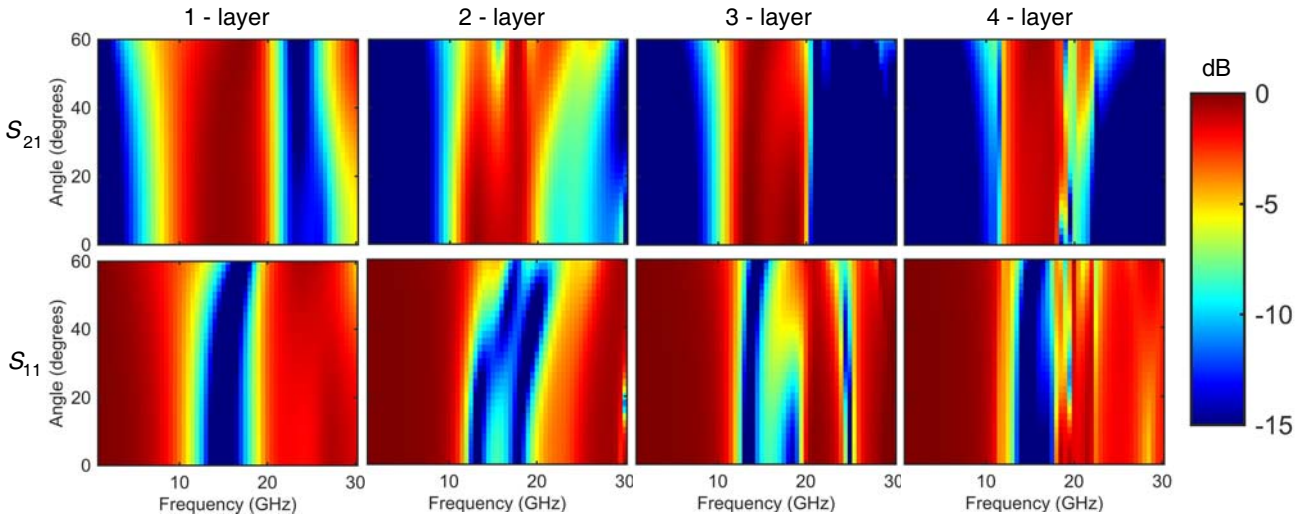

Figure 7. Transmitted and reflected amplitudes over a span of frequencies and angles for 1-layer, 2-layer, 3-layer, and 4-layer FSmSs, respectively.

is, $\vec{k}$ is directed such that $\phi = 0°$ over the range $0° \leq \theta \leq 60°$ in spherical coordinates, where $\theta = 0°$ is normal incidence and $\theta = 90°$ is grazing incidence.

The performance of the FSmS remains relatively stable out to an angle of incidence of approximately 30°, for all cases presented in Figure 7. As the angle of incidence exceeds 30° the angular stability of the response degrades for the one- and two-layer FSmSs, as shown in the S_{21} and S_{11} maps in Figure 7. In the case of three- to four-layer FSmSs, the angular response is maintained out to $\theta = 60°$, Figures 7. In addition to the robust angular response, the roll-off is consistent with the FDTD simulation at $\theta = 0°$. In principle, it should be noted that the FEM or spectral-FDTD simulations could also be coupled with the GA in order to optimize for a desired angular response with the addition of wide angle impedance matching (WAIM) layers that allow for tuning of the dielectric profile. The angular response of these FSmSs are provided by a combination of the compact lattice spacing of the arrays, dielectric profiles of the stack up, and element pattern. However, this additional dimension to the search space goes beyond the scope of this work.

3. EXPERIMENTAL VALIDATION

A 30.5 cm × 30.5 cm FSmS sample was fabricated and characterized using a free-space focused-beam system, based on the three-layer design shown in Figure 5(c). The measurement system, shown in Figure 8(a), uses two horns and two dielectric (i.e., rexolite) lenses to establish a Gaussian beam in the region between the lenses.

This field configuration is well suited for characterizing structures such as the FSmS for two reasons. First, the sample under test is placed at the waist of the Gaussian beam, where the amplitude of the field has a Gaussian taper and the phase is uniform. For a sufficiently large sample, the focused nature of the beam ensures that edge scatter is not a significant source of error in the measurements. Second, the uniform phase at the location of the sample means that the incident electromagnetic field can be approximated as a plane wave. This is important for evaluating the performance of periodic structures like the FSmS, which were designed under the assumption that the excitation is a plane wave.

The amplitude taper at the location of the sample in the system is controllable by the design of the lenses. For the configuration used to validate the performance of the FSmS, the −10 dB spot radius ranged from roughly 15 to 2.5 cm over the frequency band measured (4–26 GHz). The system was calibrated using a response isolation calibration [34]. A 1 nanosecond time gate is used to minimize the effect of multiple reflections within the system to ensure only the scattering characteristics of the FSmS is captured.

The measured values of S_{11} and S_{21} are plotted in Figure 8(b). In this figure, solid lines indicate

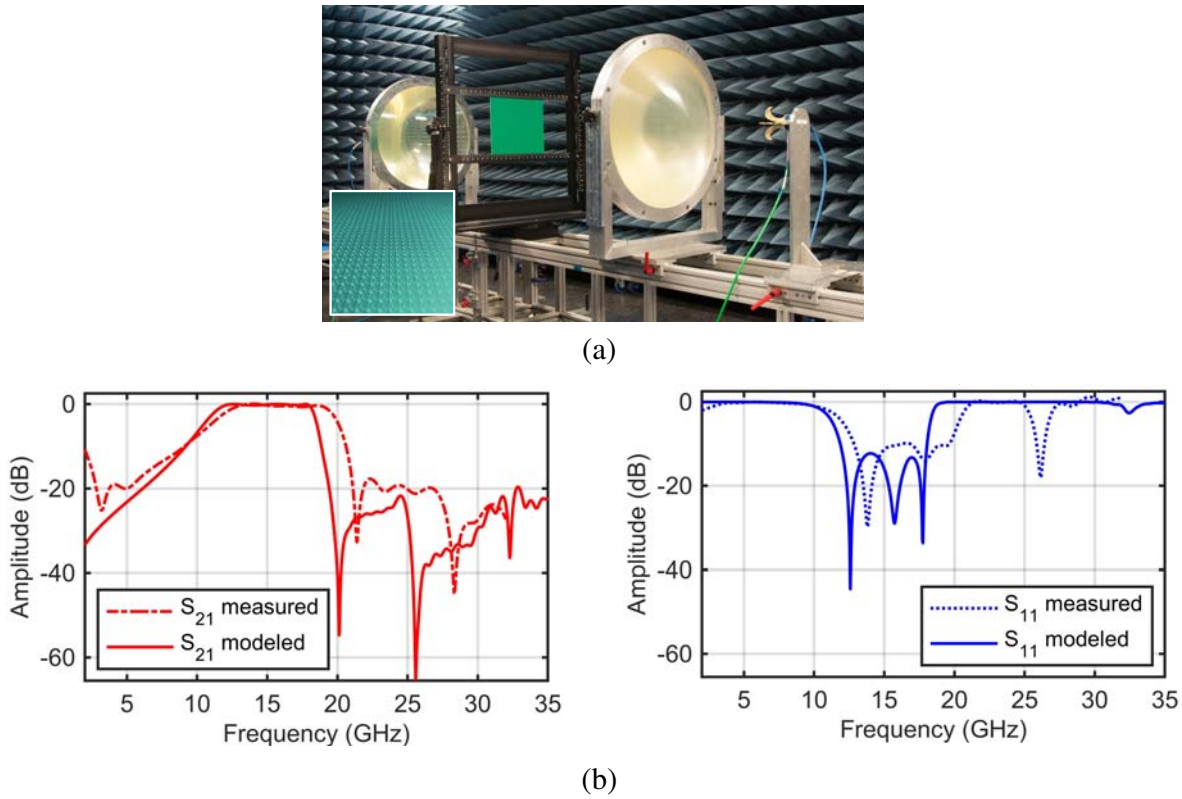

Figure 8. (a) Free-space focused-beam system, (inset) sample under test (SUT), i.e., the three-layer FSmS. (b) Direct comparison of modeled and measured scattering parameters.

modeled results, while dashed lines are measurements. S_{11} is plotted with blue lines, and S_{21} is plotted with red lines. The measured results agree well with the simulated values, giving confidence in the validity of the computational model used for the design of the metasurfaces discussed in this paper.

4. CONCLUSIONS

In this work, we have demonstrated the ability of evolutionary processes to guide designs of metasurfaces with ultra-wideband frequency selectivity. The design process can be restricted by stringent physical bounds — periodicity of the unit cell selected to forbid the excitation of higher order Floquet harmonics for a given frequency regime, thickness constrained by available footprint or fabrication tolerances, and substrate materials selected based on design goals (e.g., low-permittivity substrates for ultra-wideband applications), etc. In a similar fashion, the fitness function can be formulated in accord with basic physical principles such as perfect transmission/reflection for in- and out-of-band regions with the in-band reflection set at the Bode-Fano limit. In systematically studying one- to four-layer metasurfaces, we observed that three-layer structures are sufficient to provide a well-formed filter response with low insertion losses ($< 0.3\,\mathrm{dB}$), suppressed in-band reflection ($-12\,\mathrm{dB}$), and robust angular performance within a sub-wavelength electrical thickness ($\lambda_c/10$). These concepts, and this form factor, can be applied as a heuristic optimization technique to design metasurfaces and metamaterials from the microwave to optical regimes for passive structure or active systems with the proper modifications.

ACKNOWLEDGMENT

The authors would like to thank Dr. Ryan S. Westafer for stimulating discussions and internal peer-review of this article. The authors would also like to thank Mr. Bobby A. Blake for assistance with

graphics. This work was funded from the Georgia Tech Research Institute's independent research and development HIVE program under the direction of Mr. Benjamin Riley and Mrs. Kathy Harger; their guidance and support is greatly appreciated.

REFERENCES

1. Pendry, J. B., et al., "Extremely low frequency plasmons in metallic mesostructures," *Physical Review Letters*, Vol. 76, No. 25, 4773, 1996.
2. Pendry, J. B., et al., "Magnetism from conductors and enhanced nonlinear phenomena," *IEEE Transactions on Microwave Theory and Techniques*, Vol. 47, No. 11, 2075–2084, 1999.
3. Valentine, J., et al., "Three-dimensional optical metamaterial with a negative refractive index," *Nature*, Vol. 455, No. 7211, 376, 2008.
4. Landy, N. I., et al., "Perfect metamaterial absorber," *Physical Review Letters*, Vol. 100, No. 20, 207402, 2008.
5. Schurig, D., et al., "Metamaterial electromagnetic cloak at microwave frequencies," *Science*, Vol. 314, No. 5801, 977–980, 2006.
6. Enoch, S., et al., "A metamaterial for directive emission," *Physical Review Letters*, Vol. 89, No. 21, 213902, 2002.
7. Chen, H. T., et al., "Active terahertz metamaterial devices," *Nature*, Vol. 444, No. 7119, 597, 2006.
8. Lu, D. and Z. Liu, "Hyperlenses and metalenses for far-field super-resolution imaging," *Nature Communications*, Vol. 3, 1205, 2012.
9. Wakatsuchi, H., et al., "Circuit-based nonlinear metasurface absorbers for high power surface currents," *Applied Physics Letters*, Vol. 102, No. 21, 214103, 2013.
10. Wakatsuchi, H., et al., "Waveform-dependent absorbing metasurfaces," *Physical Review Letters*, Vol. 111, No. 24, 245501, 2013.
11. Wakatsuchi, H., et al., "Experimental demonstration of nonlinear waveform-dependent metasurface absorber with pulsed signals," *Electronics Letters*, Vol. 49, No. 24, 1530–1531, 2013.
12. Wakatsuchi, H., et al., "Responses of waveform-selective absorbing metasurfaces to oblique waves at the same frequency," *Scientific Reports*, Vol. 6, 31371, 2016.
13. Wakatsuchi, H., "Time-domain filtering of metasurfaces," *Scientific Reports*, Vol. 5, 16737, 2015.
14. Eleftheriades, G. V., "Electronics: Protecting the weak from the strong," *Nature*, Vol. 505, No. 7484, 490, 2014.
15. Xu, H. X., et al., "Tunable microwave metasurfaces for high-performance operations: Dispersion compensation and dynamical switch," *Scientific Reports*, Vol. 6, 38255, 2016.
16. Genevet, P., et al., "Recent advances in planar optics: From plasmonic to dielectric metasurfaces," *Optica*, Vol. 4, No. 1, 139–152, 2017.
17. Balthasar Mueller, J. P., et al., "Metasurface polarization optics: Independent phase control of arbitrary orthogonal states of polarization," *Physical Review Letters*, Vol. 118, No. 11, 113901, 2017.
18. Khorasaninejad, M., et al., "Polarization-insensitive metalenses at visible wavelengths," *Nano Letters*, Vol. 16, No. 11, 7229–7234, 2016.
19. Byrnes, S. J., et al., "Designing large, high-efficiency, high-numerical-aperture, transmissive metalenses for visible light," *Optics Express*, Vol. 24, No. 5, 5110–5124, 2016.
20. Filippo, C., A. Monorchio, and G. Manara, "Wideband scattering diffusion by using diffraction of periodic surfaces and optimized unit cell geometries," *Scientific Reports*, Vol. 6, 25458, 2016.
21. Xu, H. X., et al., "Flexible control of highly-directive emissions based on bifunctional metasurfaces with low polarization cross-talking," *Annalen der Physik*, Vol. 529, No. 5, 1700045, 2017.
22. Zhao, J., et al., "Fast design of broadband terahertz diffusion metasurfaces," *Optics Express*, Vol. 25, No. 2, 1050–1061, 2017.
23. Zhang, Y., et al., "Broadband diffuse terahertz wave scattering by flexible metasurface with randomized phase distribution," *Scientific Reports*, Vol. 6, 26875, 2016.

24. Miller, P., "Ka-band — The future of satellite communication," *TELE-Satellite and Broadband*, Vol. 1, No. 9, 12–14, 2007.
25. Padilla, P., "Electronically reconfigurable transmit array at Ku band for microwave applications," *IEEE Transactions on Antennas and Propagation*, Vol. 58, No. 8, 2571–2579, 2010.
26. Borji, A., D. Busuioc, and S. Safavi-Naeini, "Efficient, low-cost integrated waveguide-fed planar antenna array for Ku-band applications," *IEEE Antenna and Wireless Propagation Letters*, Vol. 8, 336–339, 2009.
27. Weile, D. S. and E. Michielssen, "Genetic algorithm optimization applied to electromagnetics: A review," *IEEE Transactions on Antennas and Propagation*, Vol. 45, No. 3, 343–353, 1997.
28. Reid, D. R. and G. S. Smith, "Design and optimization of Fresnel zone plates using a genetic algorithm and a full-electromagnetic simulator," *Microwave and Optical Technology Letters*, Vol. 51, No. 9, 2223–2227, 2009.
29. Scott, M. M., et al., "Permittivity and permeability determination for high index specimens using partially filled shorted rectangular waveguides," *Microwave and Optical Technology Letters*, Vol. 58, No. 6, 1298–1301, 2016.
30. Allen, K. W., et al., "An X-band waveguide measurement technique for the accurate characterization of materials with low dielectric loss permittivity," *Review of Scientific Instruments*, Vol. 87, 054703, 2016.
31. Monticone, F. and A. Alu, "Invisibility exposed: Physical bounds on passive cloaking," *Optica*, Vol. 3, No. 7, 718–724, 2016.
32. Maloney, J. G., R. T. Lee, and D. W. Landgren, "Genetic algorithms for fragmented aperture antennas: A complete evaluation of a 24-bit design," *Radio Science Meeting (Joint with IEEE AP-S Symposium), 2013 USNC-URSI*, 115–115, 2013.
33. Munk, B. A., *Frequency Selective Surface Theory and Design*, Wiley & Sons, New York, 2000.
34. Reid, D. R. and G. S. Smith, "A comparison of the focusing properties of a Fresnel zone plate with a doubly-hyperbolic lens for application in a free-space focused-beam measurement system," *IEEE Transactions on Antennas and Propagation*, Vol. 57, No. 2, 499–507, 2009.